Title

A Decision-Supportive Structured Light Monitoring System for Additive Manufacturing Part Surface Profiling

ISBN

9783031072574

Authors

O'Dowd, Niall M
Wachtor, Adam J
Todd, Michael D

Publication Date

2023

DOI

10.1007/978-3-031-07258-1_91

Peer reviewed

A Decision-Supportive Structured Light Monitoring System for Additive Manufacturing Part Surface Profiling

Niall M. O'Dowd[1,3], Adam J. Wachtor[2], Michael D. Todd[1(✉)]

[1] University of California San Diego, La Jolla, CA 92093-0085, USA
mdtodd@eng.ucsd.edu
[2] Los Alamos National Laboratory, Los Alamos, NM 87545, USA
[3] Additive Monitoring Systems, Lemont, IL 60439, USA

Abstract. Additive manufacturing (AM) processes are rapidly maturing and being adopted in numerous industrial sectors. One of the big challenges with many AM processes is the need for part quality control, either in post-manufactured assessment or in-situ during the build. This paper presents a low-cost structured light system (using camera and projector) that exploits digital fringe projection to achieve surface profiling of AM parts. Additionally, a probability density function of the surface profile is derived, helping the measurement process to provide the probabilistic support required for AM part quality control decisions. Results from a prototype system on AM parts are demonstrated.

Keywords: digital fringe projection, additive manufacturing, surface profiling, measurement uncertainty quantification

1 Introduction

Additive manufacturing (AM), often referred to as industrial 3-dimensional (3-D) printing, is a manufacturing technique characterized by repeatedly adding material to create an intended object [1]. The typical AM process begins with a computer-aided design (CAD) file which is then converted to a tool path, then actuated by the AM machine (often referred to as 3-D printer). Many distinct methods of AM have been invented and utilized per their individual strengths and weaknesses, though there are several features which are common among most methods, such as high designed freedom, high speed, low cost for small batches, and low investment cost. Although the earliest AM processes can be traced to stereolithography with polymers in the late 1980s, the advent of the first recognized metal AM system occurred in 1994 by EOS, dubbed the EOSINT M250, which operated via direct metal laser sintering (DMLS) [2] also known as powder bed fusion (PBF); this is currently the dominant AM tech-

nology used in the modern aerospace industry. PBF techniques include selective laser sintering (SLS) selective laser melting (SLM), and electron beam melting (EBM). These techniques utilize a similar manufacturing process, by first raking gas or water atomized metallic powder over a flat build plate within a pressurized inert gas build chamber. Then, one or more welding beams or lasers melt or sinter the powder in the pre-designated pattern calculated from the CAD part file. The build chamber lowers, and a new layer of metal powder is raked across the newly formed solid layer and surrounding un-fused powder. This process repeats for each layer of the part.

Substantial time and resources are spent after the MAM build process for final part preparation and certification. Post processing includes support structure removal, hot isostatic pressing, surface finishing, chemical treatments. Traditional quality control (QC) approaches including ultrasound, thermography, penetrant testing, eddy current, and x-ray computed tomography provide either localized or whole-part quality assessment after the part is already fully constructed, resulting in wasted fabrication time and materials if the part does not pass inspection. More importantly, the access of these inspection techniques is limited to the external faces of the manufactured part, making the quality of the internal features unknown, which may have been the driving reason for the part to be produced by MAM.

A main source of final-build defects in PBF are powder-based defects (PBDs). These defects include striations, depressions, and clumping, and can lead to detrimental part defects such as keyhole porosity formation, lack-of-fusion (LoF), and even damage to the recoater blade [3-6]. Keyhole porosity and LoF PBDs have been observed to occur in regions of powder non-uniformity, where the solidification process occurs with too much energy, or too little, respectively. Non-uniformity in powder layer thickness contributes to irregular volumetric energy density, a function of laser parameters and powder layer thickness, observed to be related to the inception of cascading keyholing and lack-of-fusion defects. Irregular powder coating also can produce out-of-plane geometrical features, resulting in chipping or skipping of the recoater blade, consequently observed to create PBDs in subsequent layers due to inadequate raking of powder across the build chamber.

A common denominator of the causes of PBDs is the localized height of the powder layer, making for a suitable in-situ measurement feature, indicative of overall part health. Digital fringe projection (DFP) [7] is a technique that uses the visible spectrum to diagnose PBDs, through measurement of the exposed powder layer and fused layer. DFP is a type of structured light sensing that uses varying light intensity patterns, e.g., fringes, projected onto the part (or un-fused powder) and a camera which captures the deformation of the incident fringes. By projecting a series of predefined patterns, a 3D model of the part's surface can be created with real-world dimensional units. The speed of this technique is limited mostly by post-processing; data acquisition time can be reduced below 3 seconds if the projector and camera frames are synchronized. The short data acquisition time make DFP suitable for implementation in closed feedback-loop control.

This paper describes a low-cost DFP system designed for surface profiling in this application, with additional development of a measurement uncertainty quantification model that gives confidence intervals on image height estimations at each pixel. Such

a design could support AM part accept/reject decision-making in accordance with standardized industrial practices.

2 Digital Fringe Projection

2.1 Measurement Process

A general schematic of a reference based DFP process is shown in Fig. 1 (left), with the physical initial prototypical implementation on the right.

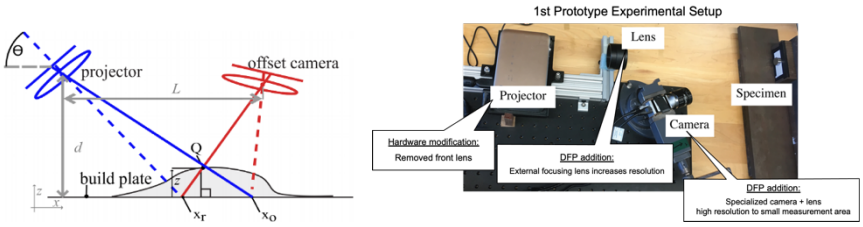

Fig. 1. General schematic of DFP (left), and physical prototype implementation (right).

In the DFP measurement process, phase measurements (an intermediate value related to height profile through a calibration routine) are made by projecting a series of patterns on to a scene and recording the resulting deformation of the patterns caused by the measured object. In Fig. 1, the point Q is the point to be measured. A common implementation of DFP is a differential phase measurement; a series of fringe images are first projected onto a flat reference plane (mathematical or physical, denoted by the subscript r in Fig. 1), and then placing the measurement object (denoted by the subscript o in Fig. 1) into the scene, which deforms the incident projected fringe pattern. The camera records images of the incident fringes on both surfaces, where the intensity $I_{(r,o)}$ of any fringe incident on the measurement surface (either r or o) at any given location $x_{(r,o)}$ is given by

$$I_{(r,o)} = A_{(r,o)} + B_{(r,o)} \cos\left(2\pi x_{(r,o)}/P\right), \tag{1}$$

where $\phi_{(r,o)} = 2\pi x_{(r,o)}/P$ is the fringe phase, P is the fringe pitch, and $A_{(r,o)}$ and $B_{(r,o)}$ are the ambient light intensity and the projected fringe contrast, respectively, at $x_{(r,o)}$. The object height z at this point is then given by a differential phase measurement between object and reference

$$z = \frac{d\,(x_o - x_r)}{L + x_o - x_r} = \frac{P\phi d}{2\pi L + P\phi}, \tag{2}$$

where $\phi = \phi_o - \phi_r$. The nonlinear encoding of phase in Eq. (1) necessitates a phase-modulation approach to recover it, so N phase-shifted images are generated and projected

onto both reference and object with equipartitioned spatial shifts $\delta_k = 2\pi k/N$, $k = 1...N$ ("bins"); it may be shown that the individual reference and object phases at the point of interest may be recovered by summing over the phase-shifted intensities:

$$\phi_{(r,o)} = \arctan\left(\frac{-\sum_{k=1}^{N} I_{(r,o),k}\sin\delta_k}{\sum_{k=1}^{N} I_{(r,o),k}\cos\delta_k}\right), \tag{3}$$

assuming that nonlinear projector gamma issues are negligible.

2.2 Uncertainty Quantification

The idealized intensities of Eq. (1) in practice are subject to pixel noise upon measurement. Using an additive model form, the measured noisy intensities are given by

$$I_{(r,o),i} = A_{(r,o)} + B_{(r,o)}\cos\left(2\pi x_{(r,o)}/P + 2\pi i/N + \phi_c\right) + \varepsilon_{(r,o),i}, i = 1\ldots N, \tag{4}$$

where ε designates the random pixel noise for the reference or object observed at the i-th bin, and the term ϕ_c is included to account for the spatial phase offset of the measurement point in relation to the projected fringe pattern. Eqs. (4) are substituted into Eq. (3) to get the measured object and reference phases, which are then subtracted to get the full differential phase measurement. Then, the phase noise κ is defined as the difference between this noisy differential measurement and the idealized differential measurement, and if quadratic noise terms inside the large parenthesis set in Eq. (3) are ignored, it may be shown that

$$\kappa \approx \arctan\left(\frac{\frac{2}{N}\sum_{i=1}^{N}\sin\left(\frac{2\pi i}{N}+\phi_c\right)\bar{\varepsilon}_{r,i} - \sin\left(\frac{2\pi i}{N}+\phi+\phi_c\right)\bar{\varepsilon}_{o,i}}{1+\frac{2}{N}\sum_{i=1}^{N}\cos\left(\frac{2\pi i}{N}+\phi_c\right)\bar{\varepsilon}_{r,i} + \cos\left(\frac{2\pi i}{N}+\phi+\phi_c\right)\bar{\varepsilon}_{o,i}}\right), \tag{5}$$

where the overbars on the noise terms just indicate normalization of the noise by the fringe contrasts. Eq. (5) may be interpreted as a noise transfer function, where pixel noise structure $\varepsilon_{(o,r),i}$ in the measured intensities gets converted to phase noise κ in the output.

Of course, this phase noise is just propagated into the surface height estimation via Eq. (2); if the height estimation error χ is defined, similar to the way the phase noise was defined, as the difference between the noisy height estimation and ideal height estimation, $\chi = z(\phi+\kappa) - z(\phi)$, then it may be shown that

$$\chi = \frac{\kappa P(d-z)^2}{2\pi L d + \kappa P(d-z)}. \tag{6}$$

If Eq. (5) were then substituted into Eq. (6), the result is a complete noise transfer function from pixel intensity to surface height error. Using change of variables formula, the probability density of χ may be found:

$$
\begin{aligned}
p(\chi) &= \frac{p(\kappa)}{|\partial\chi/\partial\kappa|} \\
&= \frac{p(\kappa)(2\pi Ld + \kappa P(d-z))^2}{2\pi LP(d-z)^2 d} \\
&= \frac{2\pi Ld\, p(\kappa)}{P(\chi+z-d)^2}
\end{aligned} \tag{7}
$$

which is a very general form result for any given probability density function of the phase noise κ, $p(\kappa)$. In [8], a probability density function for κ was derived based on the transfer function Eq. (5), and that form could be substituted into Eq. (7), where κ would be obtained by inverting Eq. (6). The full, generalized probability density function is too complex to reproduce here, but a common case occurs when the pixel intensity noise structure has no inter-projection correlation and no correlation between reference and test object data, with the same standard deviations and zero mean on each projection. This case of Eq. (7) results in

$$
p(\chi) = \frac{e^{\frac{-N}{4\left(\sigma_o^2+\sigma_r^2\right)}} Ld}{P(-d+\chi+z)^2}
\left(\frac{e^{\frac{N\cos^2\frac{2\pi L\chi d}{P(d-z)(d-\chi-z)}}{4\left(\sigma_o^2+\sigma_r^2\right)}} \sqrt{\pi}\sqrt{N\cos^2\frac{2\pi L\chi d}{P(d-z)(d-\chi-z)}} \left(\operatorname{erf}\left(\frac{1}{2}\sqrt{\frac{N\cos^2\frac{2\pi L\chi d}{P(d-z)(d-\chi-z)}}{\sigma_o^2+\sigma_r^2}} \right) \pm 1 \right)}{2\sqrt{\sigma_o^2+\sigma_r^2}} + 1 \right), \tag{8}
$$

where σ_o and σ_r are the object data and reference data pixel noise standard deviations, respectively. Eq. (8), and more generally Eq. (7), would thus be surface height χ (output) uncertainty quantification as a function of pixel noise ε (input) and system parameters.

3 Application to Power Bed Defect Detection

In this section, results showing the detection of lab-created PBDs made by the proposed DFP monitoring system, employing the accompanying uncertainty models to execute a parametric study evaluating multiple measurement parameters, are presented. The effects of varying experimental geometries (illumination angle θ, number of projections N, and fringe pitch P) to determine parameters best suited for in-situ PBD monitoring are explored.

Intentional PBDs were created using a modified recoater blade with four damage locations representative of the size and shape of PBDs which can occur in the PBF process. The “pristine” recoater blade was used to create a uniform powder bed to serve as the DFP reference surface, and the “defective” recoater blade was used to create realizations of raised-streak PBDs. The “defective” blade was fabricated with a

set of four notches, increasing in size and width, and was used to create realizations of PBDs. Each realization of PBDs were made using the same raking motion to move powder across the aluminum tray, producing an intrinsically random, but consistent surface structure (Fig. 2(left)). Four streak PBDs, of approximate heights of 150−180 μm, 105−120 μm, 45−75 μm, and 20−45μm for PBDs 1-4 shown in Fig. 2(right). A Keyence VHX-1000 height measurement microscope was used to estimate the characteristic height and width of the PBDs, considered "ground truth." The prototype DFP monitoring system was comprised of a research projector, camera, and laptop for triggering and processing images. The projector is an EKB Technologies DPME4500MKII-OX On-Axis Focusable projector; the illumination optics are the Texas Instruments DLP LightCrafterTM 4500 chipset and software package. This particular projector was selected for its variable focus, and 0% offset projection optics to allow the possibility of altering throw distance and field-of view by adding concentric lenses. A Basler Ace acA4600 GigE camera was used to capture images of projected fringes. The camera position was kept constant at viewing angle of approximately 60°, indicative of the geometries of the EOS M 290 3-D printer, a common aerospace manufacturing printer, with the center of the front lens positioned at x ≈ 7" and z ≈ 13.5". Pixel density in this study were approximately 50μm. The output triggering functionality of the projector was used to trigger camera image acquisition. This allowed the capture of fringe images at uniform intervals to eliminate projector "draw lines" which occur without synchronization. Calibration details and further experimental design considerations are given in [8].

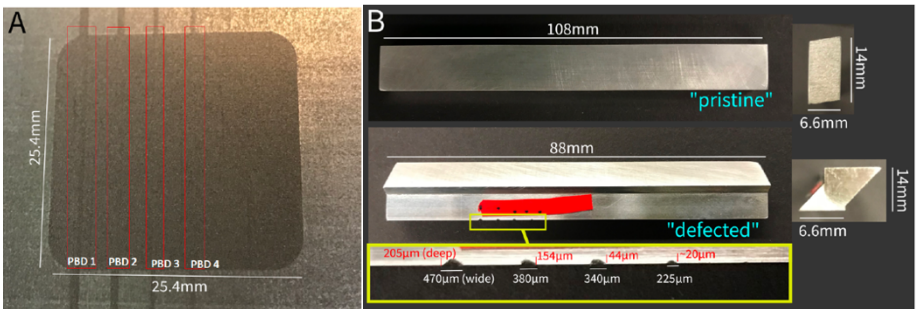

Fig. 2. General schematic of DFP (left), and physical prototype implementation (right).

To estimate the uncertainty field on DFP measurements, Eq. (8) was used to establish fundamental central tendency and dispersion characteristics of the height error,

$$E(\chi_l) = \int_{-\infty}^{\infty} \chi_l p(\chi_l) dx$$
$$Std(\chi_l) = \sqrt{\int_{-\infty}^{\infty} [\chi_l - E(\chi_l)]^2 p(\chi_l) dx}, \tag{9}$$

where χ_l is the differential height (DH) error variable. With these expressions, the ideal DH single-point standard deviation was calculated for the average level of pixel

intensity noise and used to determine the fringe P selected for each experimental set-up. For reference, the experimental fringe contrast was approximately 90 units of pixel intensity; with an average standard deviation of 1.67 pixel intensity units, that equates to an average of .0186 pixel noise (normalized by fringe contrast). Significantly higher fringe contrast was achieved for illumination angles $\theta > 25^{\circ}$, but for the sake of consistency, a contrast value achievable by all measurement angles was selected.

Figure 3 shows the selected parameters for experiment for all four illumination angles θ, all four fringe pitches P, and all five fringe projection bin numbers N. The green shaded areas correspond to DFP resultant height noise approximately 1/2 of the measured height of each PBD streak, which the authors argue is the minimum sensitivity required to detect a single pixel sized PBD with 95% confidence. The colored series lines show how the ideal standard deviation of measurement increases for increasing fringe pitch P, for a range of bin numbers N. The gray dashed lines show the selected P for each angle; each four representing similar resultant calibration constants.

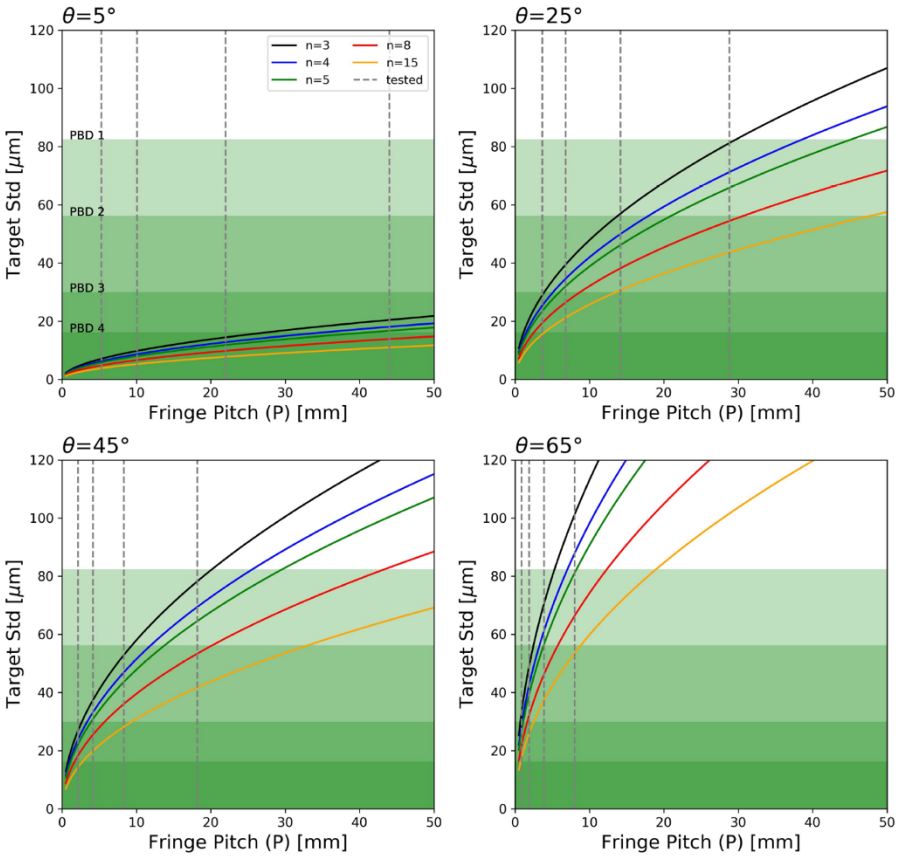

Fig. 3. Parameter selections for the experiment with varying projection count N, pitch P, and illumination angle θ. The green shaded areas show the regions of minimum required noise to resolve PBDs with heights characteristic of experiment.

To summarize our findings across every combination of tested parameters, the noise distributions of ensemble experimental DH measurements were compared to the estimated single-point uncertainty. Figure 4 shows the estimated and experimental average noise fields on DH measurements across θ,N,P. Estimated DH measurement noise is shown with filled circles and solid bars representing a single standard deviation, and the experimental full field noise median is shown with X's and error bar caps representing a single standard deviation. The green areas in the figure correspond to minimum levels of DH noise required to detect the corresponding PBD, at a 95% confidence interval for a single measurement point.

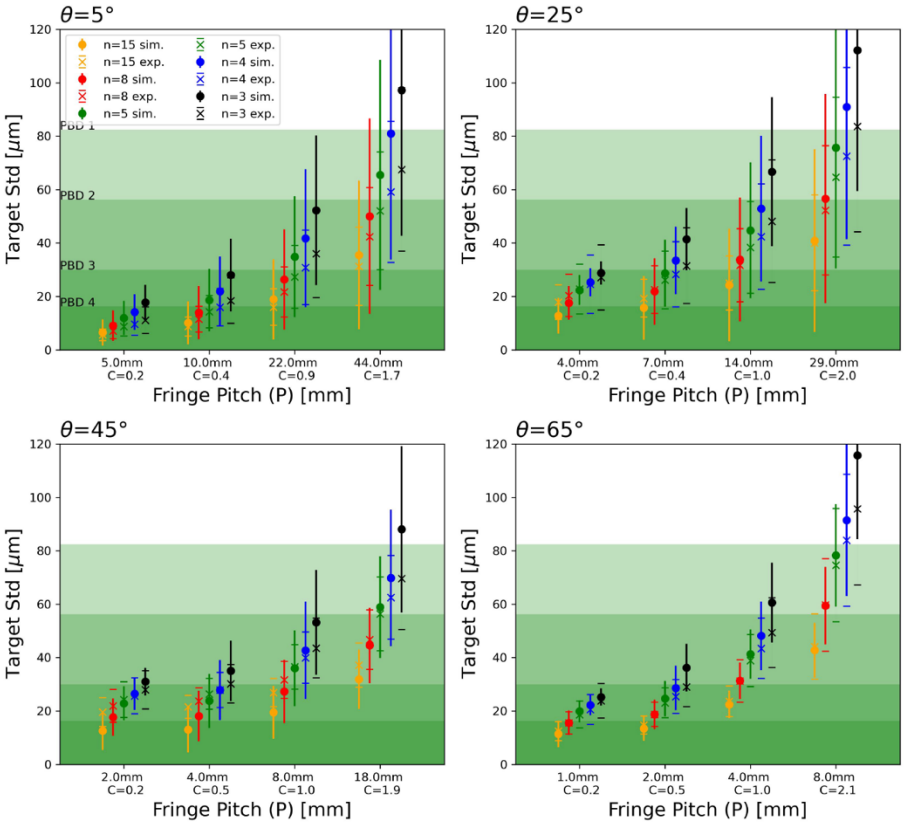

Fig 4. Measured DH noise across iterations for a range of illumination angles θ, bin number N, fringe pitch P. Green areas show the minimum experimental value of uncertainty required to detect a single pixel of the corresponding PBD at 95% (or 2σ) confidence. Experimental points are shown with error bars of a single standard deviation. Uncertainty model estimations are shown with filled circle markers.

The uncertainty model summarized the average observed noise levels of the experiments, with agreement for each parameter combination within a single standard deviation. For measurement parameters across all θ, for $N > 5$ and calibration constant $C < 1.7$, the measurement model estimated the experiment very accurately. When P in-

creases (for equivalently $C > 1$), the model begins to erroneously overestimate the measurement noise, which becomes large enough to impact the most severe PBD streaks. A higher discrepancy between the model estimations and the experimental noise for $N < 5$ was also observed, expectedly so as a results of inadequate sinusoidality of projected fringes during low bin number measurement.

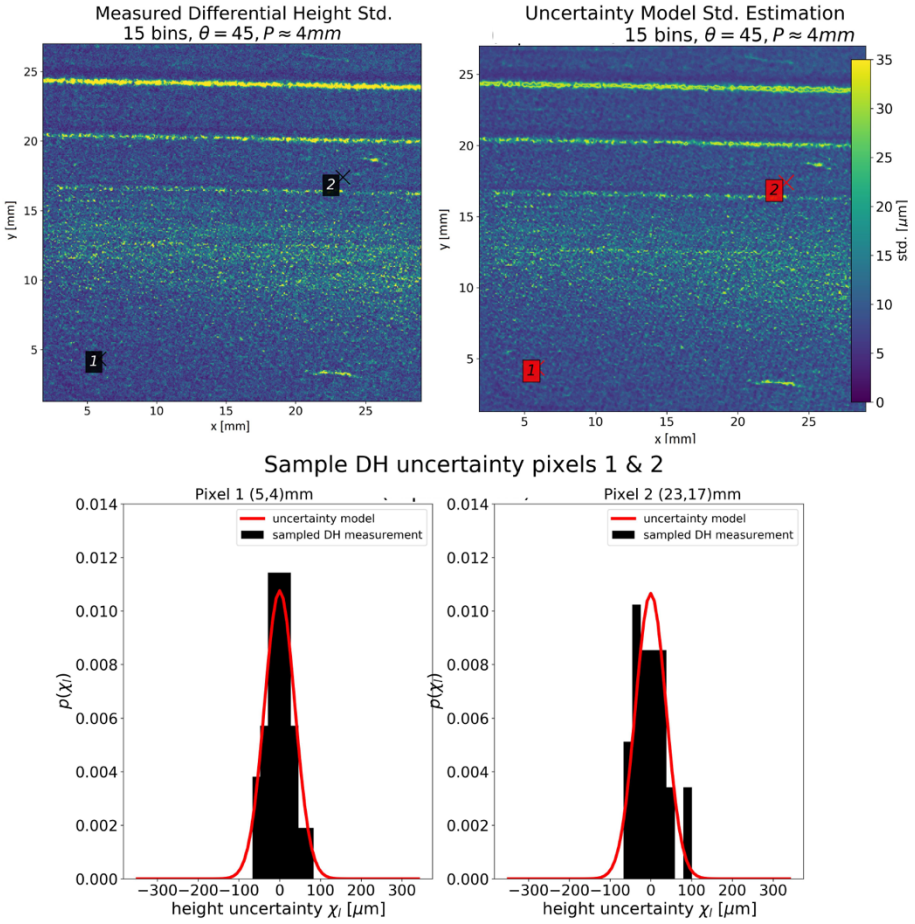

Fig. 5. Full field differential height measurement noise of an example "pristine" powder condition; upper left shows measured differential height noise across iterations, upper right shows estimated DH uncertainty made by the single point uncertainty model, and the lower shows estimated PDFs for local sample pixels 1 and 2 from the two upper sub-figures.

To showcase an example of the model's estimation of DH uncertainty, a representative case comparing observed DH noise across all 15 iterations and estimated uncertainty is presented in Fig. 5. Figure 5 (upper left) shows the measured standard deviation of DH measurements across all iterations, for an example measurement with $N = 5$, $\theta = 45\circ$, and $P \approx 17$mm. Figure 5 (upper right) shows the estimated standard devia-

tion of the PDF produced by the single point uncertainty model for the same measurement parameters. Figure 5 (lower) shows the distribution of the DH measurements and the estimated uncertainty distribution of sample points 1 and 2 from the upper subfigures. Observed in the upper left portion Fig. 5, DH measurement noise was non-uniform across the field of measurement and varied dramatically depending on subtle surface textures. The uncertainty model captured these noise structures, seen in the upper right sub-figure of Fig. 5, allowing for pixel-by-pixel statistical confidence to determine the probability of each height point. The distributions of DH noise and estimated uncertainty of example pixels 1 and 2 is shown in the lower sub-figure of Fig. 5, showcasing excellent agreement between model and simulation.

4 Conclusion

This paper described work that evaluated the feasibility of digital fringe projection (DFP) for real-time part monitoring during powder bed based additive manufacturing. A rigorous model of the effects a primary measurement error source, pixel intensity noise, was established and verified against simulation and physical experiment with excellent agreement. As PBF AM practices become increasingly adopted, the system described herein represents a prototype low-cost, decision-supportive monitoring system for part surface qualification.

References

1. ASTM. ASTM F2792–10 standard terminology for additive manufacturing technologies.
2. Kip Hanson. Metal Milestones in 3D Printing. SME (2020) (https://www.sme.org/technologies/articles/2020/march/metal-milestones-in-3d-printing/)
3. Jamison L Bartlett, Frederick M Heim, Yellapu V Murty, and Xiaodong Li. In situ defect detection in selective laser melting via full-field infrared thermography. Additive Manufacturing, 24:595–605 (2018).
4. Jamison L Bartlett, Alex Jarama, Jonaaron Jones, and Xiaodong Li. Prediction of microstructural defects in additive manufacturing from powder bed quality using digital image correlation. Materials Science and Engineering: A, page 140002 (2020).
5. Fabio Caltanissetta, Marco Grasso, Stefano Petro, and Bianca Maria Colosimo. Characterization of in-situ measurements based on layerwise imaging in laser powder bed fusion. Additive Manufacturing, 24:183–199 (2018).
6. Zhongwei Li, Xingjian Liu, Shifeng Wen, Piyao He, Kai Zhong, Qingsong Wei, YushengShi, and Sheng Liu. In situ 3D monitoring of geometric signatures in the powder-bed fusion additive manufacturing process via vision sensing methods. Sensors (Switzerland),18(4):1180 (2018).
7. Yatong An, Jae-Sang Hyun, and Song Zhang. Pixel-wise absolute phase unwrapping using geometric constraints of structured light system. Optics Express, 24(16):18445–18459, (2016).
8. Niall O'Dowd, Adam J. Wachtor, and Michael D. Todd. Effects of Digital Fringe Projection Operational Parameters on Detecting Powder Bed Defects in Additive Manufacturing. Additive Manufacturing 48(102454) (2021).